Journal of Nanobiotechnology

RESEARCH

Open Access

Sequential nanoparticle therapy targeting neutrophil hyperactivation to prevent neutrophil-induced pulmonary fibrosis

Hye-Jin Lee[1†], Na Kyeong Lee[2,3†], Jisun Kim[1†], Jungbum Kim[1], Donghyuk Seo[1], Ha Eun Shin[4], Jongsu Kim[5], June Hong Ahn[6], Se-Na Kim[7,8], Hong Sook Kim[5], Juwon Park[4*], Wooram Park[9,10*], Kyung Soo Hong[6*], Chun Gwon Park[2,3*] and Wonhwa Lee[1,10*]

Abstract

Background Pulmonary fibrosis, a major complication of severe COVID-19 and post-acute sequelae of SARS-CoV-2 infection (PASC), is driven by excessive neutrophil activation and the formation of neutrophil extracellular trap (NET).

Results This study presents a sequential nanoparticle-based therapy combining DNase-I-loaded polydopamine nanoparticles (DNase-I@PDA NPs) with Sivelestat-encapsulated PLGA nanoparticles (Siv@PLGA NPs) to target both NETs and neutrophil elastase (NE) activity. DNase-I@PDA NPs were aerosolized to the lungs, facilitating NET clearance and reducing the fibrotic microenvironment, followed by intravenous administration of Siv@PLGA NPs to inhibit NE activity and prevent neutrophil hyperactivation. In a murine model of lipopolysaccharide (LPS)-induced pulmonary fibrosis, this dual approach significantly decreased fibrotic lesions, collagen deposition, and myofibroblast activation. Notably, treatment with the nanoparticles led to substantial improvements in pulmonary function. In neutrophils isolated from COVID-19 patients, the combined nanoparticle therapy reduced circulating cell-free DNA, NET, NE, and myeloperoxidase (MPO) levels, while enhancing neutrophil viability and reducing inflammatory responses.

Conclusions These findings highlight the efficacy of DNase-I@PDA NPs and Siv@PLGA NPs in addressing both acute inflammation and chronic fibrosis by simultaneously targeting NET formation and neutrophil hyperactivation. This dual nanoparticle therapy represents a promising clinical strategy for treating COVID-19-associated pulmonary complications, including PASC, by preventing long-term fibrotic progression and promoting lung recovery.

Keywords Pulmonary fibrosis, Neutrophil extracellular traps, Aerosolized drug delivery, Chronic inflammation, Post-acute sequelae of SARS-CoV-2 (PASC)

†Hye-Jin Lee, Na Kyeong Lee and Jisun Kim have contributed equally to this work.

*Correspondence:
Juwon Park
jpark25@hawaii.edu
Wooram Park
parkwr@skku.edu
Kyung Soo Hong
number111q@ymc.yu.ac.kr
Chun Gwon Park
chunpark@skku.edu
Wonhwa Lee
wonhwalee@skku.edu
Full list of author information is available at the end of the article

Graphical abstract

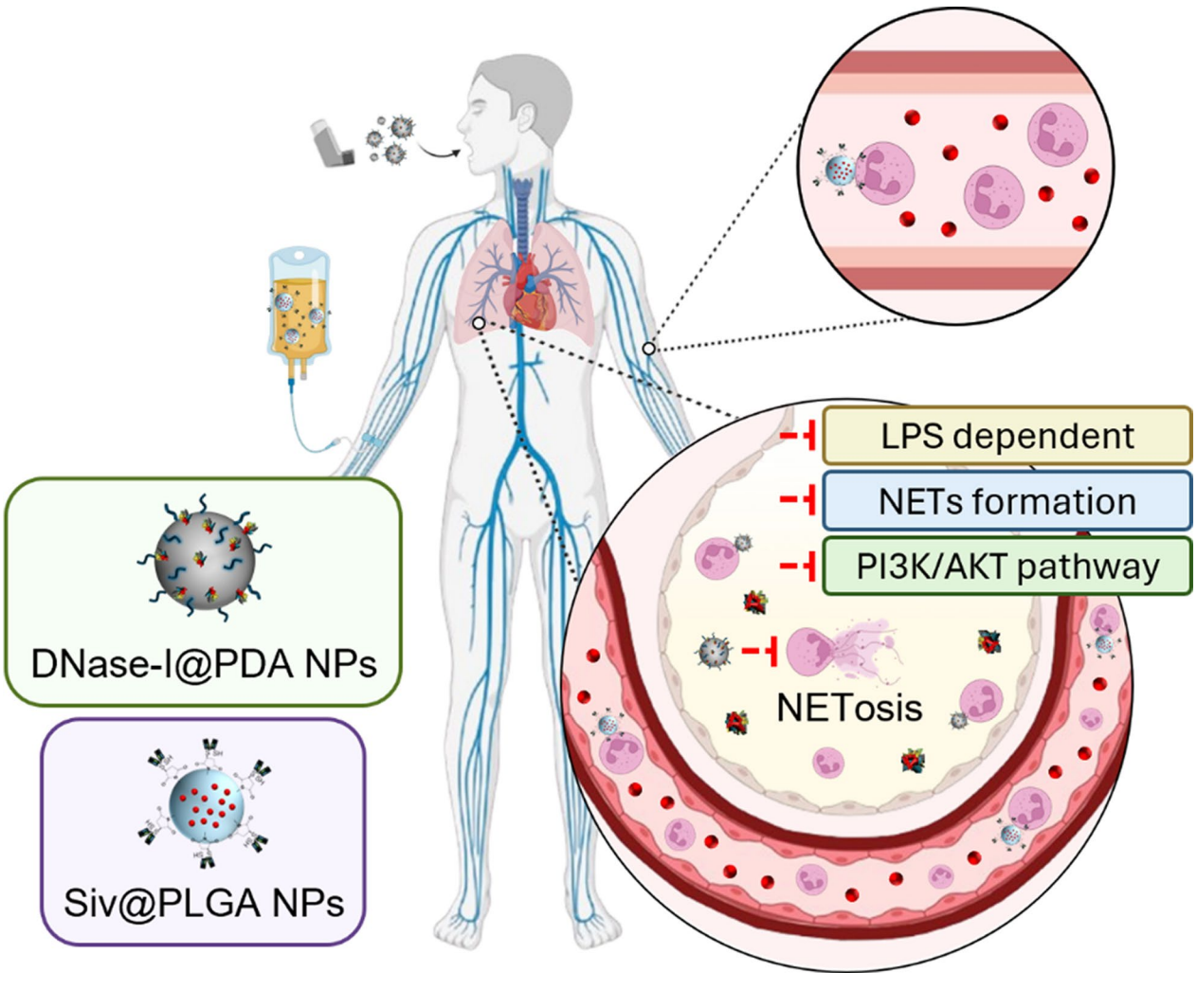

Background

Despite advances in treatment strategies through continuous endeavors after the outbreak of COVID-19, plethora of patients being declared fully cured are still suffering from the silent yet devastating aftermath of acute lung injury referred to as post-acute sequelae of SARS-CoV-2 infection (PASC) [1]. PASC is being regarded as symptoms triggered by etiologically unknown SARS-CoV-2-driven chronic inflammation including dyspnea, coughing, thoracic discomfort, fatigue and impaired pulmonary function [2]. Inasmuch as the precise mechanisms underlying PASC remain elusive, making effective treatment is daunting. As a result, clinicians often struggle with the intricacies of prescribing and resort to recommending symptomatic relief medications rather than eliminating the fundamental cause altogether. Moreover, this contributes to prolonged discomfort and pain for the patient, further adversely affecting quality of life. Thus, four years after the beginning of the COVID-19 pandemic, given that we now know the chance in which PASC occurs, it would be prudent to make prior consideration of long-term therapeutic approaches immediately after the infection to forestall the occurrence of PASC.

Among the myriad clinical manifestations of PASC, pulmonary fibrosis stands out as a particularly severe and prevalent outcome driven by alveolar damage and the accumulation of collagen-producing fibroblasts, which result in excessive extracellular matrix deposition and irreversible impairment of pulmonary function [3, 4]. While the acute inflammatory response is essential for

pathogen clearance, in severe viral infections, it can trigger unchecked inflammation and immune dysregulation, culminating in chronic immune activation [5]. This prolonged immune state is characterized by sustained production of inflammatory cytokines and the infiltration of immune cells into lung tissue, precipitating extensive tissue damage and promoting extracellular matrix deposition, thus accelerating the progression of fibrosis [6].

Recent studies have proposed that NET may influence fibrotic responses in the lung and contribute to the development of long-term pulmonary complications following viral infection, including those observed in PASC [7]. NET may activate signaling pathways in fibroblasts and epithelial cells, including TGF-β1/Smad2, β-catenin, and ERK1/2, which have been implicated in fibroblast-to-myofibroblast transition and extracellular matrix production. Suppression of miR-7, a regulator of TGF-β signaling, has also been observed in NET-rich environments, further enhancing Smad2 phosphorylation and promoting epithelial-to-mesenchymal transition (EMT) [8]. Additionally, NET components such as oxidized DNA and histones can act as damage-associated molecular patterns (DAMPs), stimulating TLR9–NF-κB and cGAS–STING pathways, which are associated with chronic inflammation and immune-mediated activation of fibrotic pathways[7, 9, 10].

As part of the systems responsible for regulating NET turnover, DNase-I has been implicated in facilitating the breakdown of extracellular DNA [11]. However, under fibrotic conditions, DNase-I activity appears to be reduced, which may delay NET clearance and result in their sustained accumulation in the lung [7]. Persistent NET burden in this context has been linked to ongoing epithelial injury, inflammatory cell recruitment, and profibrotic signaling, suggesting a potential self-reinforcing mechanism in fibrotic progression. Insights from these studies support the relevance of targeting NET stability and clearance as a potential therapeutic approach to limit inflammation-associated fibrosis in post-viral lung disease.

In this study, we put forth a novel therapeutic strategy combining localized and systemic targeting aimed at curbing neutrophil hyperactivation and aberrant NET formation during the early phase of infection, with the intent of forestalling the progression of PASC. Specifically, we explored the combined use of DNase-I and Sivelestat, an established therapeutic regimen for pulmonary fibrosis that has shown inhibitory effects on NET formation in preclinical models and alleviating lung inflammation [12]. Our approach was tailored to optimize both the timing and route of administration, ensuring maximal therapeutic effect within the inflammatory milieu that characterizes the early post-infection phase. Aerosolized DNase-I is initially administered to selectively target regions of the lung predisposed to fibrosis, thereby mitigating the excessive formation of NETs and the accumulation of circulating free DNA (cfDNA), both of which are strongly implicated in amplifying inflammatory cascades and fostering a pro-fibrotic microenvironment during the early stages of infection [13, 14]. Following this, intravenous administration of Sivelestat, a neutrophil elastase (NE) inhibitor, modulates peripheral neutrophil activity to reduce excessive neutrophil activation. By integrating both localized and systemic interventions, this strategy aims to interrupt the pathological cascade that drives inflammation and tissue damage, thereby offering a comprehensive approach to mitigating the progression of lung fibrosis in severe infectious diseases and PASC.

To address the limitations of DNase-I and Sivelestat, particularly their short half-lives and suboptimal pharmacokinetics, we developed nanoparticle formulations to extend their therapeutic efficacy and enhance targeted delivery. DNase-I, while effective in reducing NET formation, is rapidly degraded in vivo, limiting its sustained impact in modulating the pro-fibrotic microenvironment. Similarly, Sivelestat requires precise delivery to neutrophils to effectively mitigate neutrophil hyperactivation and systemic inflammation. To overcome these challenges, we fabricated DNase-I-loaded polydopamine nanoparticles (DNase-I@PDA NPs) and Sivelestat-encapsulated poly(lactic-*co*-glycolic acid) nanoparticles (Siv@PLGA NPs). In the case of Siv@PLGA NPs, we further enhanced targeting precision by conjugating $F(ab')_2$ fragments of Ly6g antibodies, which specifically bind to neutrophils, ensuring that the therapeutic agents are delivered directly to the sites of neutrophil activation. This design not only extends the duration of drug action but also minimizes off-target effects, improving overall treatment specificity.

We assessed the therapeutic efficacy of these nanoparticle formulations in both animal models and blood specimens from COVID-19 patients, showing reduction in neutrophil-driven inflammation and prevent pulmonary fibrosis. Our findings suggest that by improving the pharmacokinetics and targeting precision of DNase-I and Sivelestat, these nanoparticle-based therapies can offer a more effective and sustained intervention against the long-term sequelae of COVID-19, particularly in mitigating PASC-associated pulmonary fibrosis. This approach could pave the way for more refined therapeutic strategies in the management of post-infection complications.

Methods

Preparation and characterization of DNase-I@PDA NPs

To fabricate DNase-I@PDA NPs, PDA NPs were first synthesized following a previously reported protocol

[15]. Briefly, 180 mg of dopamine hydrochloride (Sigma-Aldrich, USA) was completely dissolved in 90 mL of deionized water (DW). Subsequently, 760 µL of 1 N NaOH was added to the solution under vigorous stirring at 50 °C, leading to a gradual color change to dark brown. After 12 h, the PDA NPs were purified by centrifugation at 17,000 rpm and washed three times with DW, followed by lyophilization. To fabricate DNase-I@PDA NPs, 50 mg of lyophilized PDA was re-suspended in 10 mL of Tris buffer (10 mM, pH 8.5) containing 25 mg of 4-arm amine-terminated PEG (Sunbio, Korea) and 25 mg of DNase-I (Roche, Swiss), and incubated under stirring at 4 °C for 4 h. Purification was performed as previously mentioned, involving centrifugation and three washes with DW, followed by lyophilization. The size, morphology, and zeta potential of the NPs were analyzed by using DLS (Zetasizer pro, Malvern Panalytical, UK) and a scanning electron microscope (SEM) Dimension ICON, Bruker, USA). The enzymatic activity of DNase-I@PDA NPs were confirmed via degradation of polymerized salmon sperm DNA (Sigma-Aldrich, USA) by gel electrophoresis [16]. For this, 0.1–200 µg of DNase-I@PDA NPs were incubated with 2 µg of salmon sperm DNA for 10 min at 37 °C, followed by agarose 1% gel electrophoresis.

Preparation of neutrophil targeted Siv@PLGA NPs

To fabricate neutrophil-targeted Sivelestat loaded PLGA nanoparticles (i.e., Neutrophil- targeted Siv@PLGA NPs), Siv@PLGA was first prepared using conventional emulsification methods [17, 18]. Briefly, 30 mg of PLGA (LG 90:10, Polysciences, USA) and 10 mg of PLGA-PEG-Maleimide (LG 50:50, PolySciTech, USA) were dissolved in 2 mL of dichloromethane (DCM). Sivelestat sodium tetrahydrate (TCI, Japan) at a concentration of 100 mg/mL in DMSO was added to the PLGA solution at 30% of the PLGA weight. The resulting polymer solution was sonicated for 10 min at 20% amplitude (140 W) using a 1 sec on-1 sec off cycle (Qsonica, USA). The resulting emulsion was then stirred at room temperature under vacuum for 1 h to completely evaporate the DCM. Siv@PLGA NPs were then collected by centrifugation at 17,000 rpm, washed three times with DW, and lyophilized. Next, to enable neutrophil targeting, the $F(ab')_2$ fragment of the anti-mouse Ly6G antibody (BioXcell, USA) was conjugated to the NPs surface. To generate the $F(ab')_2$ fragment, the antibody was cleaved using IdeS (Promega, USA) and confirmed via non-reducing SDS-PAGE. The $F(ab')_2$ fragments were then reduced with 2.5 µL of 10 mM dithiothreitol (DTT) (Sigma-Aldrich, USA) per 100 µg of antibodies to obtain free thiol groups in the hinge region. The free DTT was removed from the $F(ab')_2$ fragments by using 7 kDa MWCO desalting columns (Thermo Scientific, USA). The previously prepared NPs were re-suspended in phosphate-buffered saline (PBS, pH7.4) to a concentration of 8 mg/mL. To each milligram of particles, 25 µg of $F(ab')_2$ was added and incubated at room temperature for 1 h. The mixture was then spun down at 17,000 rpm and washed with PBS to obtain the neutrophil-targeted Siv@PLGA NPs.

Characterization of neutrophil targeted Siv@PLGA NPs

The NPs size, zeta potential, and morphology were analyzed as previously mentioned using DLS and SEM. In vitro drug release was assessed by reverse-phase high-performance liquid chromatography (HPLC). Siv@PLGA was dispersed in PBS at a concentration of 2.5 mg/mL, and 2 mL of this dispersed polymer solution was dialyzed using SnakeSkin® dialysis tubing (MWCO: 3500, Thermo Fisher Scientific, USA) against 23 mL of PBS at 37 °C with gentle shaking. At each time point, the PBS outside the tubing was collected and replaced with fresh PBS. The collected PBS was centrifuged at 17,000 rpm for 10 min, and the supernatant was analyzed by HPLC. The HPLC analysis was conducted using a 1260 Infinity II (Agilent, USA), with chromatographic separation achieved on a C18 reverse-phase column (4.6 × 150 mm, 5 µm particle size, Agilent, USA). The mobile phase comprised solvent A (0.1% Formic acid in DW) and solvent B (Acetonitrile), with a gradient elution applied as follows: 0–8 min, 20% B to 80% B; 8–12 min, 20% B. The flow rate was 1.0 mL/min, the column temperature was maintained at 30 °C, and detection was performed at 230 nm with an injection volume of 20 µL. The drug loading was measured using the same method after dissolving Siv@PLGA NPs in a 1:1 (v/v) mixture of DCM and dimethylformamide.

The conjugation efficiency of the $F(ab')_2$ fragment on the NPs surface was quantified using a BCA assay (Micro BCA Protein Assay Kit, Thermo Fisher Scientific, USA). According to the instructions, a working reagent (WR) was prepared, and 100 µL of a 2 mg/mL dispersion of Neutrophil-targeted Siv@PLGA NPs were aliquoted into a 96-well plate. An equal volume of WR was added, and the reaction was conducted at 37 °C for 2 h. To establish a standard curve, an equal volume of bare Siv@PLGA (without antibody conjugation) was used in the wells, and $F(ab')_2$ fragments were added in amounts ranging from 0 to 5 µg.

To evaluate in vitro neutrophil targeting efficiency, neutrophil-targeted PLGA NPs labeled with the lipophilic carbocyanine dye, 1,1′-Dioctadecyl-3,3,3′,3′-Tetramethylindodicarbocyanine (DiD, Biotium, USA), were co-incubated with splenocytes isolated from murine spleen, followed by flow cytometry analysis. Mouse splenocytes were seeded at 0.5×10^6 cells in PBS into a 96-well plate, and treated with 20 µg of either $F(ab')_2$ of anti-Ly6G-conjugated PLGA NPs or bare PLGA NPs. The

incubation was performed at 37 °C with shaking for 2 h. The cells were washed in PBS after co-incubation. Subsequently, the cells were labeled with fluorescence-conjugated antibodies including Zombie Aqua (Biolegend, USA) for Live/Dead staining, PE-CD45 (Biolegend, USA), APC/Cy7-Ly6g/6c (Biolegend, USA), and BV421-CD11b (Biolegend, USA). To evaluate non-specific targeting efficiency, the fluorescence of the NPs was detected in T cells and macrophages. Each cell type was labeled with Zombie Violet (Biolegend, USA), BV780-CD45 (Biolegend, USA), FITC-TCRβ (Biolegend, USA), and PE/Cy5-F4/80 (Biolegend, USA), respectively.

Animals and husbandry

5-week-old female ICR mice (Orient Bio, Republic of Korea) were used after a week of adaptation period. Under controlled temperature of 20–25 °C and humidity of 40–45%, five mice were housed per cage on a 12-h light, 12-h dark cycle. The mice were provided with a standard rodent pellet diet and had unrestricted access to water. All mice were handled in accordance with the Guidelines for the Care and Use of Laboratory Animals set forth by Sungkyunkwan University (IACUC No.: 202111291).

Aerosolized Lipopolysaccharide (LPS)-induced pulmonary fibrosis mouse model

An aerosol of LPS (E. coli O111, Sigma, USA), or same amount of PBS as a control, was intratracheally administered to anesthetized mice using a microsprayer. Each mouse was treated with 3 mg/kg LPS three times with intermissions of 12 h. Description for treatment of DNase I-PDA@NP and Siv@PLGA NP in mouse model.

Quantification of DNase-I using Enzyme-Linked Immunosorbent Assay (ELISA) in murine plasma and bronchoalveolar lavage fluid (BALF)

To obtain plasma, collected whole blood were centrifuged at 2000×*g* for 20 min. Supernatant of bronchoalveolar lavage fluid BALF was obtained after centrifuged at 1000×*g* for 10 min. Samples were coated on immunoplate and incubated overnight at 4 °C. DNase-I antibody (sc-376207, Santa Cruz, USA) was 1:1000 diluted, and loaded. The plate was incubated for 2 h at RT. 1:5000 diluted HRP-linked anti-mouse secondary antibody (Thermo Scientific, USA) was used as detection antibody. o-Phenylenediamine(OPD) was loaded as substrate, followed by being detected at 492 nm using Tecan Spark microplate reader (Tecan, Austria GmbH, Austria).

Quantification of plasma cell-free DNA (cfDNA)

To isolate cell-free DNA (cfDNA from the plasma of SARS-CoV-2-infected patients or from mouse plasma, the Qiagen QIAamp DNA Mini Blood Mini Kit was employed. This procedure was carried out in strict accordance with the manufacturer's instructions provided by Qiagen (Valencia, CA, USA). Prior to the isolation process, the plasma samples underwent centrifugation at 16,800×*g* for 10 min to remove cellular debris and ensure a clean sample for cfDNA extraction. Following isolation, the purified cfDNA was quantified using NanoDrop spectrophotometry.

Method

Complete Blood Count-For hematological analysis, white blood cell (WBC), neutrophil, and monocyte counts were measured using the Mindray BC-5000 vet automated hematology analyzer (Mindray Bio-Medical Electronics Co., Ltd., Shenzhen, China) at the Chiral Material Core Facility Center of Sungkyunkwan University. Prior to analysis, murine whole blood was collected into tubes preloaded with an appropriate volume of K_2-EDTA solution to prevent coagulation. To maintain data consistency, daily quality assurance procedures were implemented using reference controls recommended by the manufacturer.

In vivo biodistribution

The mice received aerosol administration of fluorescence-conjugated DNase-I@PDA NPs. The other group was administered fluorescence-conjugated Siv@PLGA NPs via intravenous (i.v.) injection. At specified intervals (6-, 12-, and 24-h post-administration), each group of mice was anesthetized and imaged in vivo using the Fluorescence In Vivo Imaging System (FOBI) from NEO Science (Republic of Korea). Following imaging, mice were sacrificed, and images of harvested organs were taken by the FOBI system.

Cytokine array

Cytokine profiles were evaluated using a Cytokine Antibody Array Kit (Full Moon Bio, USA). Blood samples were collected from pulmonary fibrosis (PF) mice, and plasma was isolated and stored at − 80 °C until analysis. Following the manufacturer's instructions, the antibody array membranes were blocked and subsequently incubated overnight at 4 °C with diluted plasma samples. After thorough washing, biotin-conjugated detection antibodies were applied, followed by streptavidin-HRP. Chemiluminescent detection was performed using a substrate, and signals were captured via a digital imaging system. Quantitative analysis was conducted to identify and quantify cytokines involved in the inflammatory response.

Cytokine expression values were comprehensively analyzed using R statistical software. Clustering analysis was

performed using the k-means clustering method in R. The gene sets associated with each cluster were input for pathway enrichment analysis using Metascape (https://metascape.org), and pathways with an adjusted p-value < 0.01 were selected. Additionally, genes enriched in LPS and free drugs, but not in NP, were identified by applying a significant threshold of $Log_2FC < -1$ when comparing NP to LPS and free drugs. Visualization of cytokine expression levels and principle component analysis (PCA) analysis was conducted using the ComplexHeatmap and ggplot2 packages in R.

Hematoxylin and eosin staining

Lungs from each mouse were collected, rinsed with PBS, and immersed in 4% paraformaldehyde (PFA) solution (Biosesang, Republic of Korea) at pH 7.4 for fixation. The fixation process was conducted at 4 °C for 12 h. After fixation, the lung tissues underwent dehydration through a series of sucrose solutions before being embedded in Optimal Cutting Temperature (OCT) compound and stored at − 80 °C until sectioning. The samples were then sliced into 10 μm sections and mounted onto slides. Subsequently, the slides were fixed in 4% PFA solution and stained with hematoxylin (Sigma, USA). To remove excess hematoxylin, the slides were briefly rinsed in distilled water before being counterstained with eosin (Sigma, USA). Following staining, the slides were treated with a series of ethanol and xylene solutions, then coverslipped. The images were obtained by light microscopic analysis (DM500, Leica, Germany).

Orange G staining

Processing of lung tissue samples was performed in accordance with the previously established protocol. After fixation in 4% PFA solution, the samples were thoroughly washed with PBS to remove excess fixative before proceeding to the staining process.

The lung tissue sections were then stained with hematoxylin (Sigma, USA) to visualize cellular structures and orange G-6 (Yeong Dong Diagnostics, Korea). Following staining, the slides underwent a series of graded ethanol washes to remove excess stain and were subsequently dehydrated using xylene to prepare them for mounting. Finally, the stained slides were cover-slipped using a mounting medium and analyzed under a light microscope to assess histological features.

Trichrome staining

The samples were cross-sectioned into 10 μm thick slices, which were then fixed in 4% PFA for 30 min. After fixation, the slides were sequentially stained by immersing them in Mordant in Bouin's Solution at 60 °C for 1 h, followed by Weigert's working hematoxylin for 7 min, Phosphotungstic/Phosphomolybdic Acid Solution for 10 min, and 1% acetic acid for 1 min. Post-staining, the slides underwent dehydration with two changes of 95% ethanol and two changes of 100% ethanol (2 min per change). The samples were then cleared with three changes of xylene (5 min per change) and cover slipped using permount mounting solution. Finally, light microscopic analysis of the lung specimens was performed under blinded conditions to evaluate the extent of fibrosis.

Hydroxyproline assay

Hydroxyproline levels in lung tissues were assessed using a commercially available kit (MAK008, Sigma-Aldrich). The procedure was carried out following the detailed instructions provided by the manufacturer.

Immunohistochemistry

For immunohistochemistry, frozen lung sections were initially fixed in 4% PFA solution and then washed three times with PBS. The sections were permeabilized using 0.05% Triton-X solution and blocked overnight at 4 °C in 1% BSA in PBS. The following day, the samples were incubated for 12 h at 4 °C with anti-Cit-H3 (ab5103, Abcam) and anti-NE (ab68672, Abcam) in BSA solution in PBS, gradually increasing concentrations up to 2%. After each step, the slides were washed three times with PBS to remove nonspecific binding. Subsequently, the sections were incubated at room temperature for 1 h with secondary antibodies: goat anti-rabbit Alexa Fluor 594 and 350. The slides were then washed, incubated with Sytox Green (S7020, Invitrogen) for 10 min, washed with 1X PBST, mounted with Dako mounting medium, and imaged using fluorescence microscopy (Leica, Germany).

Immunohistochemistry for α-smooth muscle actin (α-SMA) and Collagen I was performed following the same protocol as described above. For primary antibody staining, sections were incubated overnight at 4 °C with mouse anti-Collagen I (Ab34710, Abcam) and anti-α-SMA (ab7817, Abcam) antibodies diluted in blocking solution. After extensive washing with PBS, sections were incubated with secondary antibodies (goat anti-mouse Alexa Fluor 594, goat anti-rabbit Alexa Fluor 488).

Lung function assessment

The flexiVent system (SCIREQ Scientific Respiratory Equipment, Canada) was utilized to assess various lung function parameters in mice, including Elastance, Compliance, Total Lung Capacity, Inspiratory Capacity, Tissue Elasticity, Quasi-Static Compliance, and the Pressure-Volume Curve. To prepare the mice for these measurements, they were administered an injection of pancuronium bromide at a dose of 0.8 mg/kg. This compound serves as a skeletal muscle relaxant, ensuring that

the mice remained immobile during the procedure. Following euthanasia, the mice underwent orotracheal intubation using an 18 G, 30 mm catheter, which allowed for precise placement on the flexiVent system. The mice were then mechanically ventilated with forced oscillation to simulate breathing conditions. Each parameter measurement was conducted three times per mouse to ensure accuracy and reproducibility. The collected data were then recorded and calculated to provide comprehensive insights into the respiratory mechanics of the mice.

Body weight and survival rate

The survival rate and body weight of LPS-treated mice were monitored over a 480-h period following NP treatment. Body weights were measured daily using a precision balance and recorded in grams, while survival rates were assessed at regular intervals throughout the study. Mice were carefully monitored for any signs of morbidity or distress, and humane endpoints were established following institutional guidelines. Survival data were represented as percentages and plotted using Kaplan–Meier survival curves. Body weight changes were calculated relative to baseline measurements and presented as absolute values (in grams).

Sample collection and of COVID-19 patients' blood

Blood samples were collected from patients admitted to Yeungnam University Medical Center after being diagnosed with SARS-CoV-2 at a public health center in Daegu, Republic of Korea. Patients were eligible if they were over 18 years old and had an acute medical condition with at least one of the following: fever (tympanic temperature $\geq$ 38 °C at nurse triage), suspected systemic infection, two or more systemic inflammatory response syndrome (SIRS) criteria, hypotension (systolic blood pressure < 90 mmHg), or shock. Healthy volunteers were used as a control group. Clinical data were gathered for all participants, and the study was conducted following the approval of the Institutional Review Board of Yeungnam University Hospital (YUH 2020-03-057 and 2020-05-031-001). Complete blood counts were meticulously analyzed using venous blood samples collected within 24 h of the patients'admission to the hospital. Specifically, the neutrophil count was measured as part of this analysis. The assessment was performed with the aid of a Sysmex XE-2100 Automated Hematology System (TOA Medical Electronics, Japan).

NET ELISA

NETs were generated from freshly isolated neutrophils at a concentration of 1×10^5 cells. To induce the formation of NETs, the neutrophils were stimulated with phorbol-myristate acetate (PMA) (Sigma-Aldrich, USA) at a concentration of 25 nM. In parallel, control samples were treated with media composed of RPMI 1640, which was supplemented with glutamine, penicillin, and streptomycin. Following the stimulation, the production of NETs was analyzed using a fluorometric technique, as outlined in previously established protocols. The quantification of NET production was expressed in terms of arbitrary fluorescent units (AFUs), providing a standardized measure of the extent of NET formation under these experimental conditions.

MPO ELISA

Plasma samples were thoroughly analyzed to assess the extent of granule matrix protein release that occurs during the degranulation process in peripheral blood mononuclear cells (PBMCs) from both SARS-CoV-2-infected patients and mice. To achieve this, a specialized human MPO ELISA kit (BMS2038INST, Invitrogen, USA) was employed for human samples, while a corresponding mouse MPO ELISA kit (MBS700747, MyBioSource, Canada) was utilized for the murine samples.

ELISA for DNase-I activity

Plasma samples were diluted at a ratio of 1:50 and subjected to analysis using a digestion buffer that had been spiked with double-stranded DNA at a concentration of 1 μg/mL. The samples were then stained with PicoGreen, a fluorescent nucleic acid stain provided by Invitrogen (MA, USA), following the detailed instructions outlined in the manufacturer's protocol. After the staining process, the samples were incubated at 37 °C for a duration of 5 h. Following incubation, the reduction in PicoGreen staining was assessed by measuring the fluorescence emission (Em) using a fluorometer. This reduction in fluorescence provided a quantitative measure of the changes in DNA content within the plasma samples under the experimental conditions.

Statistical analysis and software

Each experiment was conducted independently a minimum of three times. Statistical significance was assessed via the unpaired t-test, and all analyses were carried out using GraphPad Prism software. Results are presented as mean ± SEM, with a significance threshold of $P < 0.05$. P-values and additional experimental details are outlined in the figure legends. R statistical software (version 4.3.2) was used for comprehensive analysis of cytokine array data. Visualization of cytokine expression levels and PCA analysis were performed using the ComplexHeatmap and ggplot2 packages in R.

Results

NPs preparation and characterization

The PDA NPs were synthesized through the oxidative polymerization of dopamine hydrochloride in an alkaline aqueous solution. This process was initiated by adjusting the pH with NaOH, followed by auto-oxidation under ambient air conditions, as illustrated in Scheme 1 (Scheme 1) [15]. Subsequently, following our previously established method [19–21], DNase-I and PEG were co-immobilized onto the surface of PDA NPs through a single-step procedure. This process exploits the reactivity of catechol and quinone groups on the PDA surface. The primary amine groups of DNase-I and the terminal amine groups of PEG formed covalent bonds with the PDA surface via Schiff base formation and Michael addition reactions, resulting in stable surface functionalization. Additionally, neutrophil-targeted Siv@PLGA NPs were prepared using a conventional emulsification method and subsequently conjugated with $F(ab')_2$ fragments of an antibody specific for neutrophils [22]. The morphology of the particles, as observed via SEM, was uniformly spherical (Fig. 1A). Additionally, the sizes of the PDA and DNase-I@PDA NPs, measured by DLS, were approximately 199 and 184 nm, respectively, with minimal size variation attributable to the binding of PEG and DNase-I to the surface (Fig. 1B). The sizes of PLGA and Siv@PLGA NPs were found to be 274 and 273 nm, respectively. This minimal difference in size indicates that the incorporation of Sivelestat into the PLGA nanoparticles did not significantly alter their dimensions. The zeta potentials of PLGA and Siv@PLGA NPs were −11.13 and − 11.87 mV, respectively, showing minimal variation (Fig. 1C). In contrast, PDA and DNase-I@PDA NPs exhibited zeta potentials of − 11.33 mV and − 17.92 mV, respectively, with DNase-I@PDA NPs displaying approximately 36% more negative charge. This increased negative charge is due to the binding of negatively charged DNase-I to the surface of PDA NPs [23, 24]. The release profile of Sivelestat from Siv@PLGA NPs was quantified over time using HPLC (Fig. 1D). The drug loading achieved was 163 μg of Sivelestat per mg of PLGA NPs, yielding an encapsulation efficiency of 54%. As shown in Fig 1D, Sivelestat demonstrated a sustained release from the PLGA NPs over a 24-h period. The DNA degradation enzymatic activity of DNase-I@PDA NPs were evaluated using agarose gel electrophoresis (Fig. S1). While 2 U of free DNase-I completely degraded 2 μg of DNA, DNase-I@PDA NPs achieved complete degradation of the same amount of DNA at concentrations above 5.0 μg. These results demonstrate that the DNase-I immobilized on the PDA NPs surface retains its effective DNA degradation capability.

Neutrophil-targeted Siv@PLGA NPs were prepared by conjugating the $F(ab')_2$ fragment of the anti-Ly6g antibody, which targets neutrophils, to the Siv@PLGA NPs. To achieve this, the anti-Ly6g antibody is cleaved into $F(ab')_2$ and Fc fragments using the protease IdeS [17, 22]. The cleavage of the antibody was confirmed by non-reducing SDS–PAGE gel stained with Coomassie Brilliant Blue, where bands corresponding to $F(ab')_2$ and Fc were observed at 115 and 25 kDa, respectively (Fig. S2). After cleavage, the hinge region of the $F(ab')_2$ fragment is reduced with DTT to generate thiol groups, which then conjugate with the maleimide groups on the particle surface. The conjugation efficiency of the antibody to the particle surface was subsequently verified using a BCA assay. It was determined that 17.5 μg of antibody was bound per 1 mg of NPs, corresponding to 70% of the antibody used in the reaction being conjugated to the particle surface.

The targeting efficiency by the antibody conjugation to surface of PLGA NPs was assessed in vitro using flow cytometry with fluorescently labeled PLGA NPs in mouse splenocytes (Fig. 1E). The intensity shifts of DiD was compared between cells treated with DiD-loaded neutrophil-targeted PLGA NPs and cells treated with bare PLGA NPs, with untreated cells as baseline. In the case of target cells, neutrophils, the shift in DiD signal increased by 19% when treated with neutrophil-targeted PLGA NPs, which is approximately five times higher than that observed with DiD-loaded bare PLGA NPs. This indicates that the conjugation of antibodies to the surface of PLGA NPs enhances the targeting efficiency towards neutrophils. Additionally, to evaluate non-specific binding of the PLGA NPs, DiD signal shifts were examined in non-target cells, such as T cells and macrophages. The results showed that neutrophil-targeted PLGA NPs exhibited a slightly higher signal shift (approximately 2%) compared to bare PLGA NPs in both T cells and macrophages, indicating that non-specific binding of the neutrophil-targeted PLGA NPs is minimized.

Next, we analyzed time-dependent degradation of DNase-I@PDA NP in murine serum to evaluate its enzymatic persistence. The results showed that DNase-I levels peaked at 6 h post-treatment, suggesting that the nanoparticle formulation effectively maintained DNase-I activity during the early phase after administration. After reaching its peak, DNase-I levels steadily decreased. A significant drop was detected at 12 h post-treatment, which indicates continuous enzymatic degradation. By 24 h following treatment, DNase-I levels were no longer detectable within this timeframe. This observation

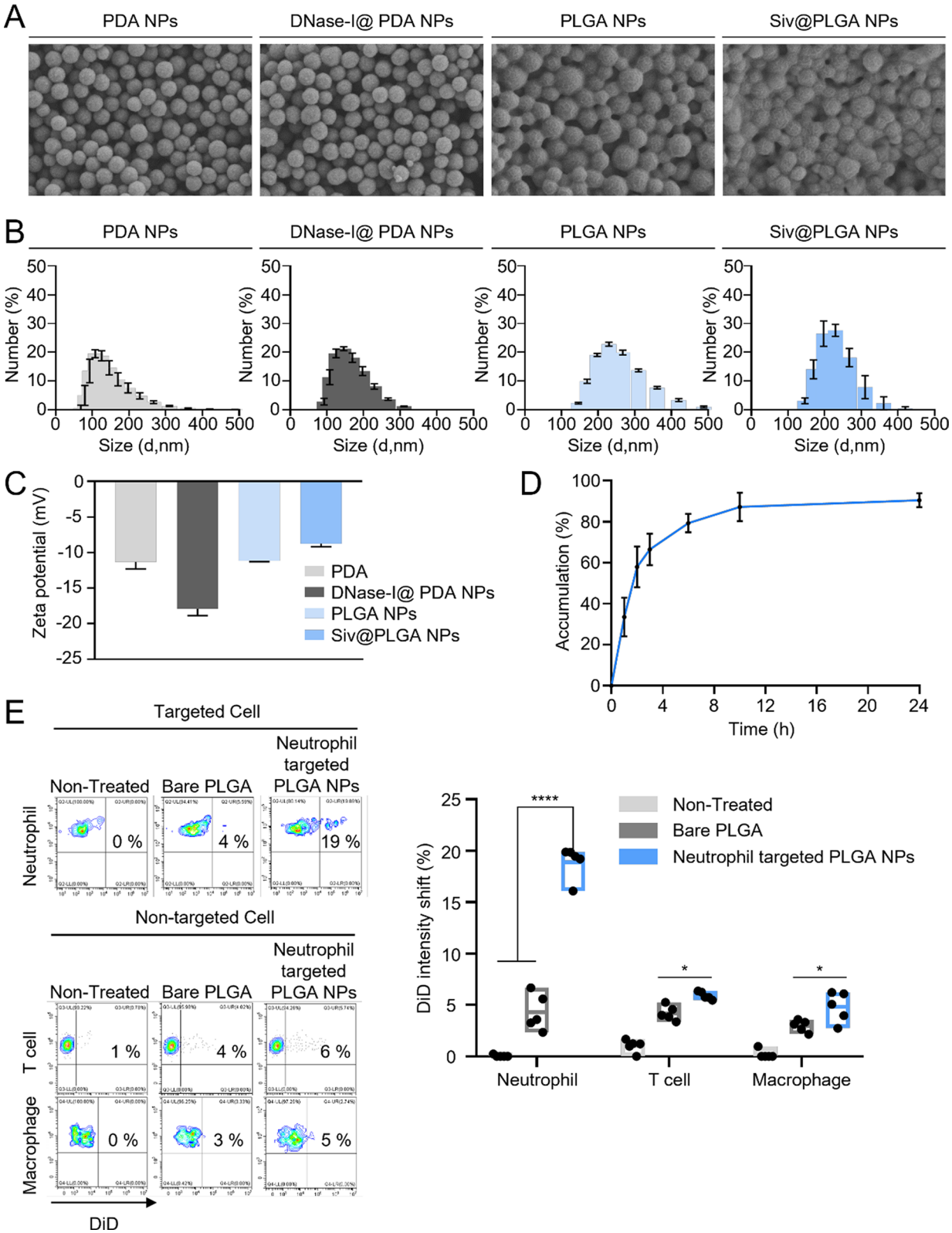

Fig. 1 Characterization of NPs. **A** SEM image (n = 3, Scale bar = 500 nm) **B** Size and **C** Zeta potential (n = 3) of PDA, DNase-I@PDA, PLGA, and Siv@PLGA NPs. **D** Drug release profile of Siv@PLGA NPs (n = 4). **E** In vitro targeting efficiency of Neutrophil targeted PLGA NPs (n = 5). Statistical analysis was performed using a two-tailed unpaired t-test. Data are presented as mean ± SEM. * $P < 0.05$, ** $P < 0.01$, *** $P < 0.001$, **** $P < 0.0001$ (*v.s.* LPS)

demonstrates that the nanoparticle-conjugated DNase-I had undergone complete degradation. (Fig. S3).

These findings imply that DNase-I@PDA NPs remain active for a limited but sufficient duration to exert their enzymatic function before being naturally degraded, aligning with the expected pharmacokinetics of enzyme-based therapies. The observed degradation pattern suggests that DNase-I@PDA NPs provide a therapeutic window that allows for effective NET degradation while minimizing the risk of prolonged systemic exposure, which could potentially reduce off-target effects.

To assess the therapeutic potential of the nanoparticle formulations under inflammatory conditions resembling infection-induced lung injury, we established an in vitro transwell co-culture system that models the crosstalk between endothelial and alveolar compartments with a focus on neutrophil-mediated responses. Human endothelial cells (hy926) were seeded in the upper chamber, while human lung fibroblasts (MRC5) were placed in the lower chamber. LPS was applied to the entire system to induce a pro-inflammatory environment (Fig. S4 A). Following 12 h of LPS exposure, free DNase-I or DNase-I@PDA NPs were administered into the lower chamber to simulate alveolar delivery of therapeutics. One hour later, neutrophils were introduced into the upper chamber alongside either free Sivelestat or Siv@PLGA NPs, modeling systemic drug administration and neutrophil recruitment from circulation into inflamed lung tissue.

Under these conditions, neutrophils were anticipated to become activated and migrate toward the lower compartment in response to LPS-driven cues. Notably, treatment with nanoparticle formulations resulted in a measurable reduction in neutrophil infiltration (Fig. S4B), suggesting a potential role in tempering activation or migratory responsiveness. A concurrent decrease in cfDNA levels within the upper chamber supernatant over time (Fig. S4 C) further implied suppression of NET formation, which has been implicated in amplifying fibroblast activation through extracellular signaling. To better understand the functional consequence of this modulation, we examined the early fibrotic response in fibroblasts by measuring α-SMA levels in MRC5 lysates. Western blot analysis revealed that, in contrast to untreated conditions where α-SMA expression was elevated at early time points following LPS and neutrophil exposure, NP-treated groups did not exhibit this early induction (Fig. S4D). This early suppression may reflect a favorable alteration in the cellular microenvironment—potentially linked to reduced exposure to neutrophil-derived signals such as NETs or inflammatory proteases. Building on these in vitro findings, we proceeded to evaluate the therapeutic efficacy of the nanoparticle formulations in vivo to further validate their impact under physiologically relevant conditions.

Amelioration of acute immune responses in LPS-induced lung injury through early administration of DNase-I

In previous study, we demonstrated that the activity of DNase-I may decrease in the immediate aftermath of COVID-19 infection, potentially contributing the complications such as the formation of NETs and eventual increase of disease severity [19]. Based on these observations, we hypothesized that early intratracheal administration of DNase-I@PDA NPs could compensate for reduced DNase-I activity and attenuate the rapid accumulation of NET-derived DNA within the pulmonary system. This strategy was anticipated to prevent excessive inflammatory responses that contribute to acute lung injury. Additionally, intravenous administration of Siv@PLGA NPs, by inhibiting NE activity, was designed to suppress peripheral neutrophil hyperactivation, thereby preventing the sustained inflammatory escalation despite neutrophil infiltration into lung tissue (Fig. 2A).

To confirm the validity, we performed an investigation to determine whether aerosol injection of free DNase-I (D group) or DNase-I@PDA NPs (D@P group) decrease activation of inflammation mediators in pulmonary fibrosis mouse model induced by serial intratracheal injections of LPS. We assessed the levels of DNase-I and various immune factors in an animal model at early, intermediate, and late stages, which we hypothesized correspond to the development of post-infectious pulmonary fibrosis (Fig. 2B, C). Regarding DNase-I levels, the results indicated a significant decrease in DNase-I concentration in both murine plasma and BALF 48 h after direct intratracheal administration of LPS (Fig. 2D). Additionally, we noted an increase in the neutrophil population in the blood (Fig. S5), along with a decrease in monocyte infiltration into the BALF (Fig. 2E). This observation implies a shift in immune cell dynamics throughout the inflammatory response. By 72 and 96 h post-LPS injection, DNase-I levels in plasma showed a significant rebound compared to the 48 h time point (Fig. S6), mirroring our previous observations [19] of elevated DNase-I in severe COVID-19 patients. DNase-I levels in the BALF remained reduced throughout the 96 h period, despite the systemic rebound observed in the plasma (Fig. 2F, G). However, it is worth noting that treatment with free DNase-I and DNase-I@PDA NPs effectively restored DNase-I levels in the BALF (Fig 2F, G). DNase-I@PDA NPs achieved a more sustained elevation of DNase-I levels compared to free DNase-I, likely due to the enhanced release profile of DNase-I. Moreover, a marked reduction in blood neutrophil levels and monocyte infiltration into the BALF was observed in the D and D@P group. Immunohistochemical (IHC) analysis of monocytes also showed that the LPS group exhibited a greater presence of monocytes beyond the vascular boundary. In comparison, monocyte

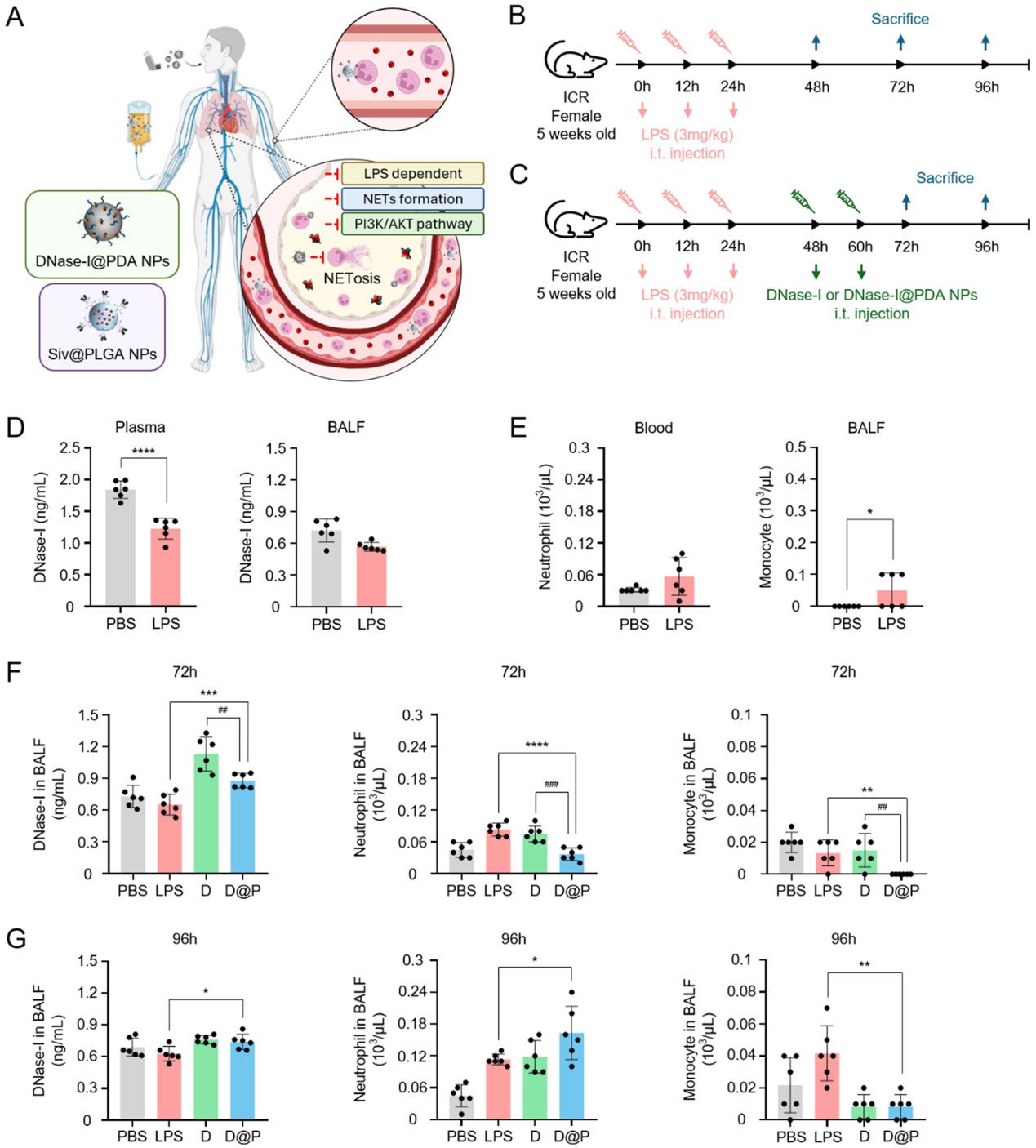

Fig. 2 Early administration of DNase-I ameliorates acute immune response in the case of COVID-19 infection. **A** Schematic of DNase-I@PDA NPs and Siv@PLGA NPs administration. **B** Schematic of LPS injection and sacrifice schedule. Mice were intratracheally (i.t.) administered three times with LPS (3 mg/kg) and sacrificed at every 24 h interval. **C** Schematic of LPS injection and treatment schedule. Mice were intratracheally (i.t.) administered three times with LPS (3 mg/kg) and were intratracheally (i.t.) administered twice with free DNase-I (D group) or DNase-I @NP (D@P group) at 24 h after the third injection of LPS. Mice were sacrificed at 12 h after the final administration of free DNase-I or DNase-I@NP at every 24 h interval. **D** Concentration of DNase-I in blood and BALF. **E** Neutrophil count in blood and BALF. **F** Immune cell populations in BALF at 72 h post-administration. **G** Immune cell populations in BALF at 96 h post-administration. Statistical analysis was performed using a two-tailed unpaired t-test. Data are presented as mean ± SEM. * $P < 0.05$, ** $P < 0.01$, *** $P < 0.001$, **** $P < 0.0001$ (*v.s.* LPS), $^{\#\#}P < 0.01$, $^{\#\#\#}P < 0.001$ (*v.s.* D + S)

infiltration appeared reduced in both the D and D@P-treated groups. Such histological evidence is consistent with the observed decrease in monocyte levels within the BALF and supports the possibility that the treatment may help temper monocyte-associated inflammatory activity (Fig. S7). These findings suggest that early administration of DNase-I, particularly in its nanoparticle formulation, may help restore DNase-I levels in the context of pulmonary fibrosis and influence immune cell dynamics, including neutrophil and monocyte populations, which play important roles in the inflammatory cascade associated with fibrotic progression.

Pulmonary retention and coadministration of DNase-I@PDA NPs and Siv@PLGA NPs

Following the demonstrated efficacy of DNase-I formulations in attenuating acute lung inflammation, we sought to explore the synergistic therapeutic effects of co-administration of DNase-I@PDA NPs and Siv@PLGA NPs in vivo. Our primary objective was to assess pulmonary retention, systemic distribution, and potency of these nanoparticles to exert both localized and systemic anti-inflammatory effects, particularly in the setting of persistent inflammation and fibrosis.

To visualize nanoparticle biodistribution and pulmonary retention, fluorescence(Cy7)-conjugated DNase-I@PDA NPs and Siv@PLGA NPs were administered according to the outlined experimental scheme (Fig. 3A). Fluorescence imaging of lung tissues revealed sustained pulmonary localization of aerosol-administered DNase-I@PDA NPs, with a gradual decrease in fluorescence intensity over 24 h post-administration. This extended retention supports the hypothesis that inhalation delivery ensures effective deposition and persistence of DNase-I@PDA NPs within pulmonary tissue (Fig. 3A), enhancing their therapeutic window in mitigating early inflammatory processes. This result is also consistent with the previously conducted in vitro DNase-I degradation experiment (Fig. S3).

Siv@PLGA NPs, delivered intravenously, were primarily expected to target peripheral neutrophils and inhibit NET formation upon migration into pulmonary tissues (Fig. 1E). While hepatic accumulation is an expected outcome due to the liver's role in nanoparticle clearance, efficient entry to the lungs was also successfully achieved (Fig. 3A). Fluorescence tracking showed that NP-bound neutrophils migrated to the lungs within 6 h of administration, suggesting effective neutrophil targeting. The continued presence of Siv@PLGA NPs in peripheral tissues indicates that they may contribute to regulating systemic neutrophil activity, which could help limit excessive NET formation and reduce inflammation in the lungs.

Cytokine profiling and pathway analysis in LPS-induced lung fibrosis models developed according to the scheme (Fig. 3B) showed that treatment with DNase-I@PDA NPs and Siv@PLGA NPs (NP group) significantly modulated inflammatory and fibrotic responses compared to the LPS and DNase-I and Sivelestat (D+S) groups (Fig. S8). PCA identified distinct cytokine expression patterns, with NP-treated animals showing enrichment in cluster 4, indicating a unique immunomodulatory effect (Fig. S9). Pathway analysis of differentially expressed cytokines indicated a marked suppression of proinflammatory and profibrotic pathways, including extracellular matrix organization, cell migration, as well as the PI3 K-Akt, NF-κB, and MAPK signaling pathways. Notably, NP treatment suppressed key chemotaxis-related cytokines such as MCP-2, GRO, PF-4, and LD78beta, critical for neutrophil recruitment and NET formation. This NET inhibition, along with the regulation of cytokine-cytokine receptor interactions and chemokine signaling, reflects the potential anti-inflammatory and anti-fibrotic effects of DNase-I@PDA NPs and Siv@PLGA NPs. This outcome underscores their potential role in controlling fibrosis and facilitating lung tissue recovery in fibrotic conditions (Fig. 3C).

Pertaining to the impact of the nanoparticles on neutrophil activation and the inflammatory mediators released by neutrophils, the combined administration of DNase-I@PDA NPs and Siv@PLGA NPs was associated with a marked reduction in neutrophil infiltration in the

(See figure on next page.)

Fig. 3 Coadministration of DNase-I and Sivelestat nanoparticle and drug release. **A** Ex vivo imaging of dissected organs after the i.v. administration of Cy7- Siv@PLGA NP and the i.t. administration of Cy7- DNase-I PDA@NP. **B** Schematic of LPS injection and treatment schedule. Mice were intratracheally (i.t.) administered three times with LPS (3 mg/kg). DNase-I PDA@NP was administrated intratracheally and Siv@PLGA NP was administrated intravenously, alternating 12 h apart. Mice were sacrificed at 48 h after the final administration of Siv@PLGA NP. **C** Heatmap illustrating the top 50 cytokines identified from a cytokine array analysis across the treatment conditions: LPS, DNase-I combined with Sivelestat (D + S), and each nanoparticle treatment (NP). The color scale denotes relative expression levels, with red indicating upregulation. Pathway enrichment analysis revealed significant involvement of inflammatory and immune-related pathways, including cytokine-cytokine receptor interaction, chemokine signaling, and the MAPK signaling pathway. **D** Neutrophil counts, **E** NET ratio, **F** DNase-I activity, **G** Concentration of NE, **H** MPO activity, and **I** cfDNA in murine BALF. Statistical analysis was performed using a two-tailed unpaired t-test. Data are presented as mean ± SEM. $^{*}P < 0.05$, $^{**}P < 0.01$, $^{***}P < 0.001$, $^{****}P < 0.0001$ (*v.s.* LPS), $^{\#}P < 0.05$, $^{\#\#}P < 0.01$, $^{\#\#\#}P < 0.001$ (*v.s.* D + S)

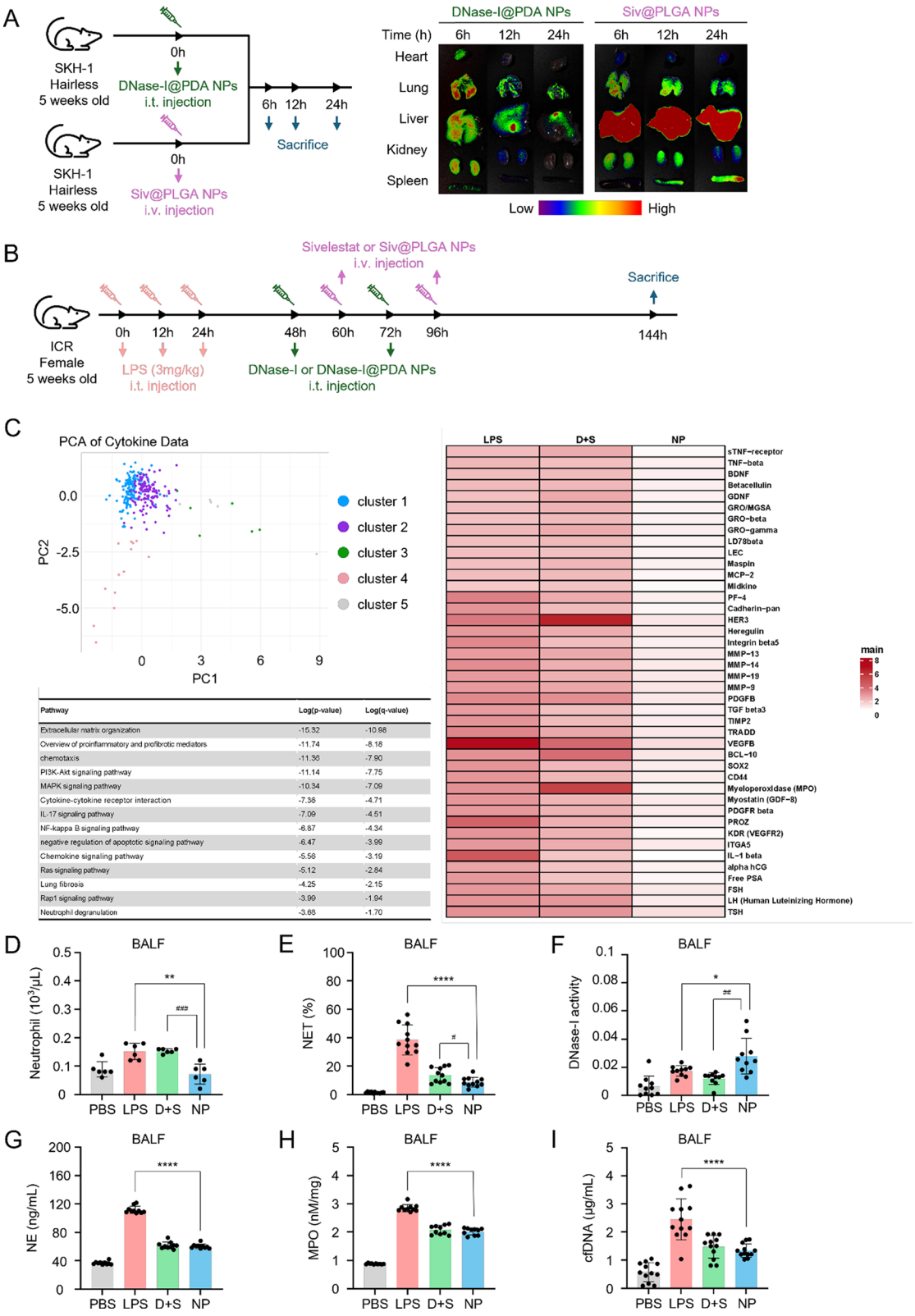

Fig. 3 (See legend on previous page.)

BALF (Fig. 3D). This reduction was accompanied by a significant decrease in NET formation in the lungs (Fig. 3E), demonstrating the efficacy of the treatment in suppressing excessive neutrophil activity. Significantly, DNase-I enzymatic activity remained stable across the treatment period, confirming that nanoparticle formulation did not impair its functionality (Fig. 3F). Co-administration with Siv@PLGA NPs led to a further reduction in NE and MPO levels, which may have contributed to NET inhibition and enhanced the anti-inflammatory effect. Since NE and MPO are associated with extracellular matrix degradation and fibrosis progression, this reduction may have played a role in modulating these processes (Fig. 3G, H). The combined treatment also led to a decrease in circulating cfDNA levels, which are considered markers of immune dysregulation and have been linked to chronic inflammation and fibrosis (Fig. 3I and Figs. S10, 11). The reduction in NE and MPO levels, along with the decrease in cfDNA in both plasma (Fig. S12) and BALF, indicates that co-administration may help regulate acute inflammatory responses and limit pathways associated with fibrotic progression.

Relieved pathological phenotypes of pulmonary fibrosis in vivo

To evaluate the therapeutic efficacy of DNase-I@PDA NPs and Siv@PLGA NPs in the context of pulmonary fibrosis, we conducted detailed histopathological and functional assessments. Histological analysis using H&E staining revealed that NP-treated mice exhibited significant restoration of alveolar structure and a marked reduction in pneumonic damage compared to untreated LPS-exposed mice (Fig. 4A). Orange G staining revealed pronounced extracellular matrix deposition in LPS-treated lungs, with NP demonstrating superior efficacy in reducing matrix accumulation compared to D+S group, as evidenced by histological patterns most closely resembling PBS controls. (Fig. 4B). Cit-H3 and NE, well-established markers of NETs, were analyzed in pulmonary vascular tissue to assess the efficacy of nanoparticles in inhibiting NET accumulation and their potential role in preserving vascular integrity via IHC staining. In LPS group, prominent Cit-H3 and NE signals were observed within the vasculature, indicating persistent intravascular NET accumulation, inefficient NET clearance, and potential endothelial dysfunction driven by neutrophil-mediated cytotoxicity. This accumulation may indicate sustained neutrophil activation and prolonged inflammatory signaling, contributing to endothelial damage. In contrast, D+S and NP groups exhibited markedly reduced Cit-H3 and NE deposition in the vasculature, suggesting that the treatment effectively mitigated neutrophil hyperactivation and excessive NET release. This reduction in intravascular NET burden implies improved NET clearance mechanisms and decreased neutrophil-induced endothelial injury. These findings highlight the therapeutic potential of DNase-I@PDA NPs and Siv@PLGA NPs to attenuate neutrophil-driven vascular inflammation and improve (Fig. 4C). Trichrome staining further confirmed a reduction in collagen deposition, with both the area and intensity of collagen expression significantly diminished in NP-treated group, indicating that the treatment effectively limited collagen accumulation, a hallmark of fibrosis (Fig. 4D). Another IHC analysis demonstrated reductions in the expression of collagen I and α-SMA in the lungs of NP-treated mice. The decreased collagen I level suggests reduced vascular inflammation and fibrotic remodeling, helping to preserve lung architecture by preventing vascular occlusion. Additionally, suppression of α-SMA expression indicates that NP treatment effectively inhibited myofibroblast activation, a critical process in extracellular matrix remodeling and tissue stiffening (Fig. 4E). The reduction in collagen I and α-SMA expression was also quantitatively confirmed through real-time PCR analysis (Fig. S13). To further corroborate these findings, we measured hydroxyproline levels as a proxy for collagen synthesis. Hydroxyproline levels were significantly lower in the NP-treated group, suggesting reduced fibrotic activity and a decreased risk of progressive fibrosis (Fig. 4F). These results suggest that the treatment mitigates the pathological remodeling associated with fibrosis by maintaining structural integrity within the lungs.

Pulmonary function assessments were conducted to investigate the physiological impact of NP treatment on respiratory mechanics in the LPS-induced lung injury

(See figure on next page.)

Fig. 4 Improved respiratory function by administrating of DNase-I@PDA NPs and Siv@PLGA NPs. **A** H&E analysis of lung tissue from LPS-induced pulmonary fibrosis mouse model. (Scale bar: 200 μm). **B** Orange G staining images. (Scale bar: 200 μm). **C** Immunohistochemistry (IHC) analysis (Cit-H3, NE, and Sytox-Green™) of lung sections of LPS-induced pulmonary fibrosis mouse model. (Scale bar: 40 μm). **D** Trichrome stained images of murine lung tissue. (Scale bar: 200 μm). **E** IHC analysis of fibrotic markers (collagen I and α-SMA). (Scale bar: 100 μm). **F** Measurement of hydroxyproline content. **G** Inspiratory capacity, lung resistance, compliance, and elastance ascertained by FlexiVent forced oscillation technique at endpoint. **H** PV curve. **I** Body weight of LPS-induced pulmonary fibrosis mouse model. **J** Survival rate of LPS-induced pulmonary fibrosis mouse model. Statistical analysis was performed using a two-tailed unpaired t-test. Data are presented as mean ± SEM. $^{*}P < 0.05$, $^{**}P < 0.01$, $^{****}P < 0.0001$ (*v.s.* LPS), $^{\#\#}P < 0.01$, $^{\#\#\#\#}P < 0.0001$ (*v.s.* D + S)

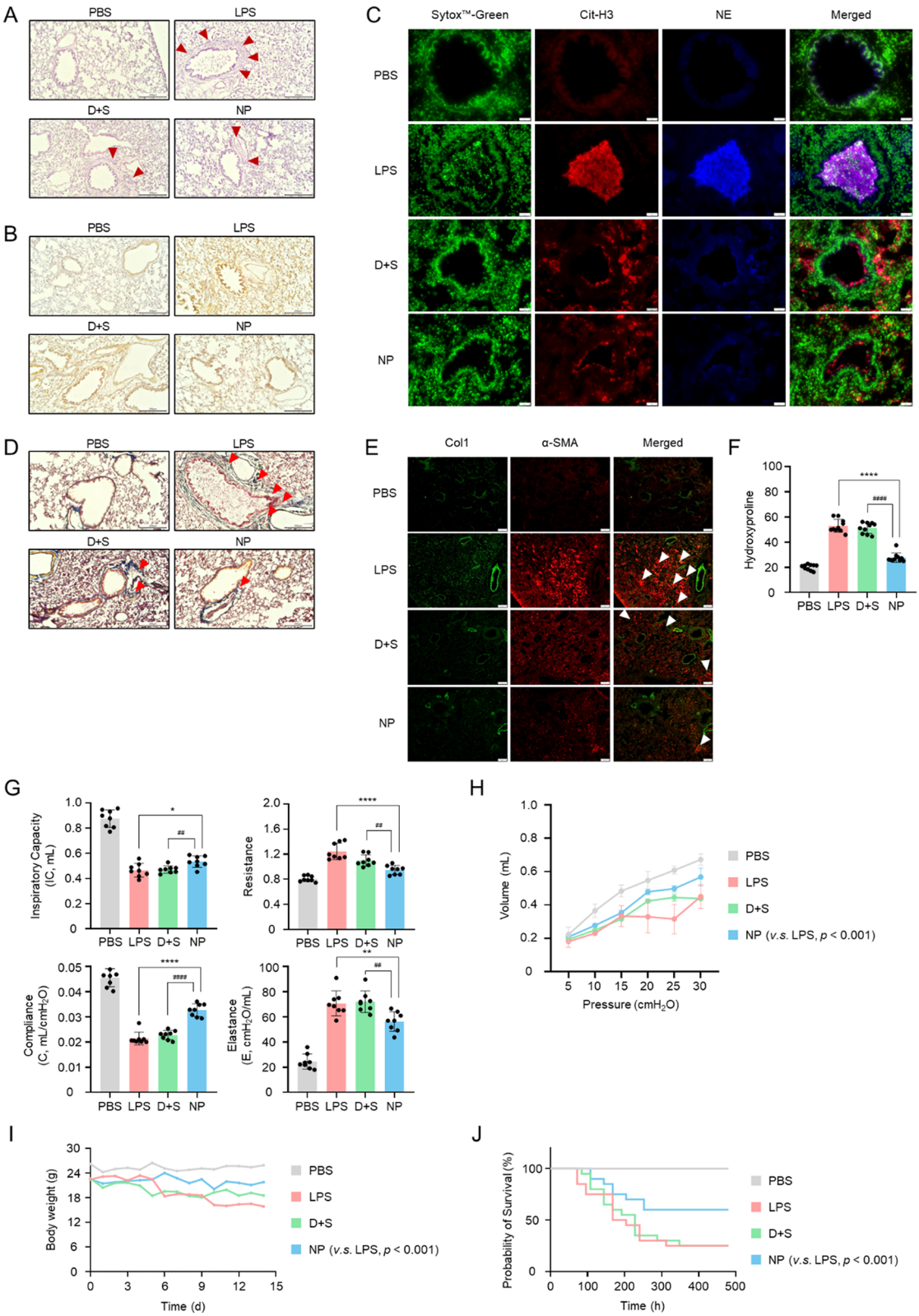

Fig. 4 (See legend on previous page.)

model. LPS-treated mice exhibited a reduction in inspiratory capacity (IC), along with increased elastance (E) and decreased compliance (C), indicating impaired lung distensibility and increased tissue stiffness—features commonly associated with fibrotic remodeling (Fig. 4G). A reduction in IC reflects a limitation in the volume of air drawn into the lungs during inspiration. Elevated elastance and reduced compliance further support the presence of restricted mechanical expansion, as these measures describe the lung's resistance to inflation and its ability to stretch under pressure. These functional impairments were further reflected in the pressure–volume (PV) curves, which were shifted downward in the LPS group, indicating reduced lung inflation capacity under applied pressure (Fig. 4H). Subsequent administrations of NPs were associated with trends toward improvement, as indicated by a modest recovery in IC and gradual normalization of E and C parameters (Fig. 4G). Correspondingly, The PV curves of NP-treated mice showed an upward shift compared to those of the untreated group (Fig. 4H). Together, these results provide evidence that NP administration contributed to the recovery of pulmonary mechanics by mitigating the functional consequences of inflammation-induced fibrotic injury.

In terms of overall physiological outcomes, NP-treated mice showed significant improvements in body weight maintenance and survival rates compared to untreated LPS-exposed controls. Mice in the NP-treated group experienced less weight loss and demonstrated a substantial increase in survival rates, underscoring the effectiveness of the treatment in mitigating the detrimental effects of LPS-induced lung injury and fibrosis (Fig. 4I, J). These results collectively demonstrate the potential of DNase-I@PDA NPs and Siv@PLGA NPs to attenuate both acute and chronic pathological features of pulmonary fibrosis, restoring lung structure and function while improving survival outcomes in treated animals.

Therapeutic efficacy of nanoparticles on neutrophils of COVID 19 patients

After confirming the in vivo restorative effects of the co-administration of DNase-I@PDA NPs and Siv@PLGA NPs, we extended our investigation to assess the therapeutic potential of these nanoparticles on neutrophils isolated from COVID-19 patients. Our results indicated that both free drug formulations and drug-encapsulated NPs contributed to a reduction in circulating cfDNA levels, which have been associated with inflammatory responses and immune dysregulation in COVID-19 patients (Fig. 5A). When DNase-I@PDA NPs were introduced to plasma samples from COVID-19 patients, we observed a notable enhancement in DNase-I enzymatic activity, suggesting that the nanoparticle formulation improved the degradation of extracellular DNA and enhanced the overall therapeutic potential in reducing cfDNA levels (Fig. 5B). Further analysis of neutrophil samples revealed that treatment with DNase-I@PDA NPs and Siv@PLGA NPs led to a substantial reduction in NET formation, as well as significant decreases in NE and MPO activity (Fig. 5C–E). These findings indicate that formulations of the nanoparticles are highly effective at suppressing neutrophil hyperactivation and limiting the downstream enzymatic processes that contribute to pulmonary tissue damage and inflammation. In addition, NP treatment markedly improved neutrophil viability (Fig. 5F), demonstrating the ability of the nanoparticles to stabilize immune cell function under inflammatory conditions. This improvement in neutrophil stability is particularly important in promoting immune homeostasis in the context of severe viral infections such as COVID-19. Collectively, these results suggest that DNase-I@PDA NPs and Siv@PLGA NPs exhibit strong therapeutic potential in mitigating the harmful effects of NETosis and reducing the risk of long-term fibrotic complications in COVID-19 patients.

Discussion

In this study, we demonstrated that the sequential co-administration of DNase-I@PDA NPs followed by Siv@PLGA NPs represents a potent therapeutic strategy for alleviating pulmonary inflammation and fibrosis. Our findings underscore the importance of early intervention, beginning with the observation that DNase-I levels significantly decrease immediately after infection, thereby promoting the formation of NETs and contributing to excessive inflammation. Early supplementation of DNase-I@PDA NPs supported extracellular DNA clearance in the lungs, leading to a reduction in NET formation and the fibrotic microenvironment. Subsequently, the administration of Siv@PLGA NPs targeted NE via the neutrophil-specific Ly6g antibody's Fab region, contributing to the modulation of NE activity and an extended therapeutic effect. This two-step approach showed the potential to regulate neutrophil hyperactivation and limit the pathological progression toward pulmonary fibrosis (Figs. 1 and 2).

The treatment was associated with a reduction in the expression of immune mediators such as NETs, NE, and MPO, which are produced by activated neutrophils and contribute to both acute and chronic inflammatory states (Fig. 3). In an in vivo fibrosis model, the sequential administrations of NPs were observed to reduce fibrotic lesions, suggesting a potential protective effect against tissue remodeling and injury (Fig. 4). The therapeutic effects were not limited to animal models, as the

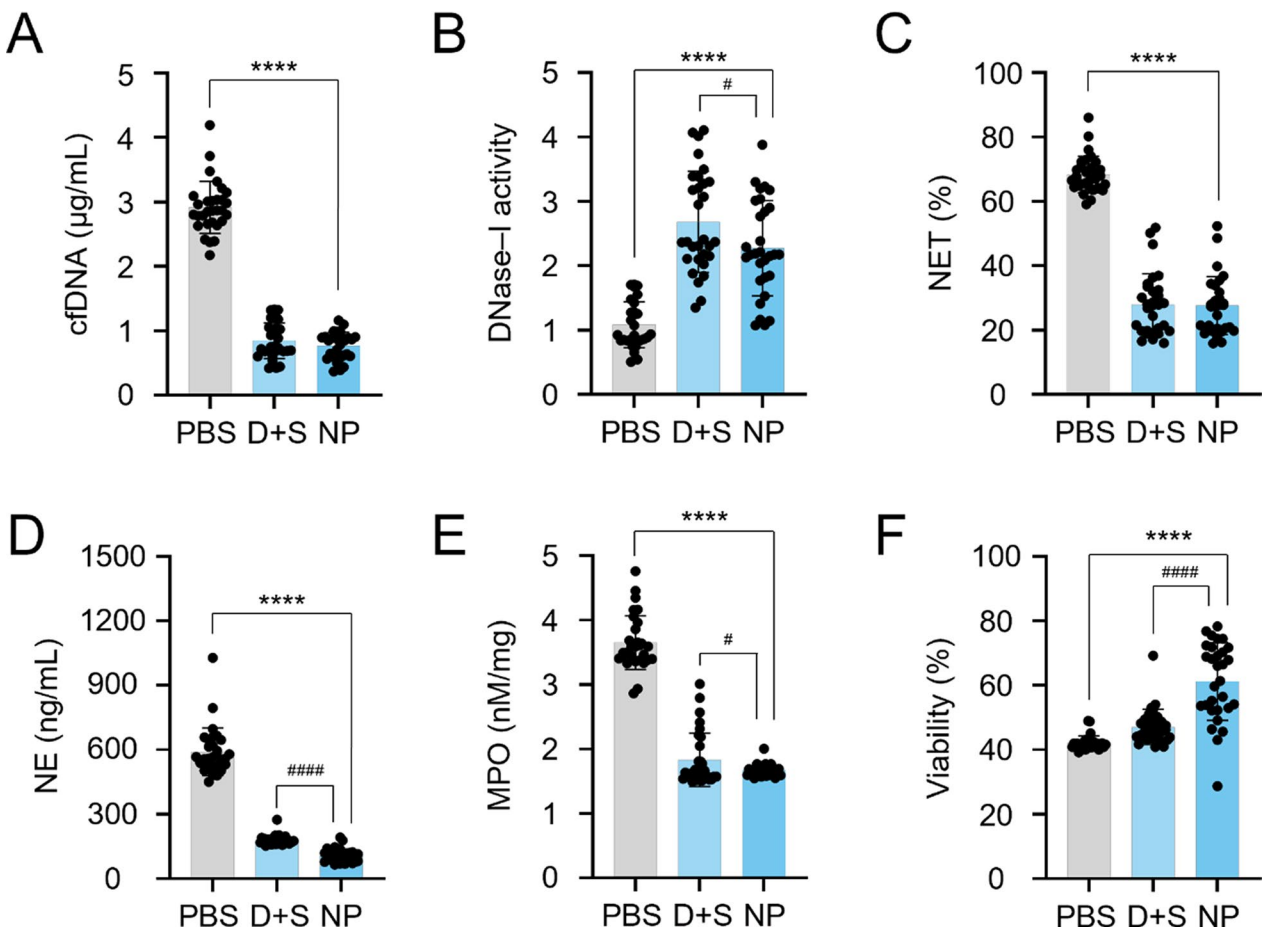

Fig. 5 Evaluation of NETosis following coadministration of free drugs and NPs in the blood of SARS-CoV-2 patients. **A** Circulating cfDNA. **B** DNase-I enzymatic activity. **C** NET formation index in PBMCs. **D** NE activity. **E** MPO activity. **F** Viability of the neutrophils. Statistical analysis was performed using a two-tailed unpaired t-test. Data are presented as mean ± SEM. $^{*}P < 0.05$, $^{****}P < 0.0001$ (*v.s.* PBS), $^{\#}P < 0.05$, $^{\#\#\#\#}P < 0.0001$ (*v.s.* D + S)

nanoparticle regimen also showed beneficial outcomes in neutrophils isolated from patients with COVID-19 (Fig. 5). These results broaden the potential clinical relevance of this nanoparticle-based dual approach beyond preclinical models and suggest its possible utility in managing COVID-19-related pulmonary complications, including PASC.

Monotherapy with DNase-I or Sivelestat has shown limited efficacy in addressing the multifaceted nature of pulmonary inflammation and fibrosis, particularly in the context of chronic conditions like lung fibrosis. Based on our findings, a sequential, multi-targeted approach appears to be more effective in modulating the progression of fibrosis. The dual mechanism of action provided by DNase-I@PDA NPs and Siv@PLGA NPs offers complementary mechanisms of action that engage distinct aspects of the inflammatory cascade. First, DNase-I@PDA NPs, administered directly to the lungs through aerosol delivery, facilitate the breakdown of extracellular DNA and NETs, which are known to contribute to sustained inflammation by forming structural and immunological barriers. Next, systemically delivered Siv@PLGA NPs target peripheral neutrophils, limiting their activation and reducing their subsequent infiltration into the lungs, which may help attenuate ongoing inflammatory responses even after neutrophil recruitment has occurred.

This combined strategy contributes to the attenuation of acute inflammation and also helps limit long-term tissue remodeling and fibrosis associated with sustained neutrophil activation. By targeting both the upstream generation of NETs and the downstream effects of neutrophil hyperactivation, the approach offers a broader means of addressing pulmonary injury in both acute and chronic phases. Notably, the sequential administration of DNase-I and Sivelestat appeared to enhance therapeutic outcomes beyond those observed with either agent alone, providing both early and prolonged modulation of inflammatory and fibrotic responses. From a clinical perspective, Sivelestat, although only approved

in select regions (China, Japan, and Korea) for treating pulmonary dysfunction [25], has demonstrated potent anti-inflammatory properties, supporting its broader applicability in conditions such as PASC. Given that neutrophils play a pivotal role in the prolonged inflammatory response observed in PASC [26], our sequential approach of DNase-I followed by Sivelestat is designed to directly engage this pathophysiological mechanism. The initial clearance of NETs by DNase-I, followed by the inhibition of NE activity by Sivelestat, contributes to reducing inflammation and limiting further tissue injury. This, in turn, lowers the likelihood of fibrotic progression and supports the maintenance of pulmonary function over time. Additionally, the combined delivery strategy offers a targeted means of addressing both the clinical manifestations and the underlying drivers of chronic pulmonary fibrosis associated with PASC.

In this context, the dual approach offers a cohesive therapeutic framework that has the potential to address both the acute inflammatory response and the subsequent fibrotic remodeling observed in COVID-19-related pulmonary complications. By sequentially targeting key neutrophil-driven mechanisms, the co-administrations of these nanoparticle formulations present a therapeutically relevant strategy that may be applicable not only to PASC but also to other fibrotic lung conditions characterized by persistent inflammation. Taken together, these findings provide a basis for further exploration of neutrophil-targeted nanotherapies in the broader context of chronic pulmonary disease management.

Conclusions

COVID-19-associated pulmonary fibrosis remains a severe long-term complication, urgently requiring effective treatments. This study presents an innovative nanoparticle-based therapy targeting both neutrophil activation and NETs) formation. Sequential administration of DNase-I-loaded polydopamine nanoparticles and Sivelestat-encapsulated PLGA nanoparticles significantly reduced pulmonary fibrosis by clearing NETs and inhibiting NE. This approach addresses both acute inflammation and chronic fibrosis, improving lung function. Our findings open new possibilities for treating various lung diseases, including PASC, and represent a significant milestone in translating nanomedicine to clinical applications. This dual-action nanoparticle strategy offers a promising path to prevent long-term fibrotic progression and promote lung recovery in COVID-19 patients and beyond.

Abbreviations

PASC	Post-acute sequelae of SARS-CoV-2 infection
DNase-I@PDA NPs	DNase-I-loaded polydopamine nanoparticles
Siv@PLGA NPs	Sivelestat-encapsulated PLGA nanoparticles
NE	Neutrophil elastase
MPO	Myeloperoxidase
NETs	Neutrophil extracellular traps
D@P	DNase-I@PDA NPs
i.t. injection	Intratracheal injection
i.v. injection	Intravenous injection
PCA	Principal component analysis
cfDNA	Cell-free DNA
IHC	Immunohistochemistry
α-SMA	α-Smooth muscle actin
TLC	Total lung capacity
IC	Inspiratory capacity
PV loop	Pressure–volume loop
E	Elastance
C	Compliance

Supplementary Information

The online version contains supplementary material available at https://doi.org/10.1186/s12951-025-03421-y.

Supplementary Material 1.

Acknowledgements

We extend our gratitude to the other contributors to this work.

Author contributions

H.-J.L., J.K., J.P., W.P., K.S.H., C.G.P., and W.L. designed the research; H.J.L., N.K.L., J.K., J.K., and D.S. performed the experiments; H.-J.L., N.K.L., J.K., J.K., H.E.S., J.H.A., S.-N.K., H.S.K., K.S.H, and W.P. analyzed the data; and H.J.L., J.K., and W.L. wrote the paper. All authors reviewed the manuscript.

Funding

This work was supported by a grant of the Korea Health Technology R&D Project through the Korea Health Industry Development Institute (KHIDI), funded by the Ministry of Health & Welfare, Republic of Korea (No. RS-2023-00266015), and by the National Research Foundation of Korea (NRF) grant funded by the Korea government (MSIT) (No. 2021R1C1C2006896).

Availability of data and materials

No datasets were generated or analysed during the current study.

Declarations

Ethics approval and consent to participate

This study was approved by the Ethics Committee of Yeungnam University Medical Center, and all participants provided consent to participate (YUH 2020-03-057 and 2020-05-031-001). This research received approval from the Ethics Committee of Sungkyunkwan University, and all procedures with animal models followed established ethical standards (IACUC No.: 202111291).

Consent for publication

Consent for publication is not applicable.

Competing interests

The authors declare no competing interests.

Author details

[1]Department of Chemistry, Sungkyunkwan University, Suwon 16419, Republic of Korea. [2]Department of Biomedical Engineering, Institute for Cross-Disciplinary Studies (ICS), Sungkyunkwan University, Suwon 16419, Republic of Korea. [3]Department of Intelligent Precision Healthcare Convergence, ICS, Sungkyunkwan University, Suwon 16419, Republic of Korea. [4]Department of Tropical Medicine, Medical Microbiology and Pharmacology, John A. Burns School Medicine, University of Hawai'i at Manoa, Honolulu 96813, USA. [5]Department of Biological Sciences, Sungkyunkwan University, Suwon 16419, Republic of Korea. [6]Division of Pulmonology and Allergy, Department of Internal Medicine, College of Medicine, Yeungnam University and Regional Center for Respiratory Diseases, Yeungnam University Medical Center, Daegu 42415,

Republic of Korea. [7]Research and Development Center, MediArk Inc., 1, Chungdae-ro, Seowon-gu, Cheongju, Chungcheongbuk 28644, Republic of Korea. [8]Department of Industrial Cosmetic Science, College of Bio-Health University System, Chungbuk National University, Cheongju, Chungcheongbuk 28644, Republic of Korea. [9]Department of Integrative Biotechnology, Sungkyunkwan University, Suwon 16419, Republic of Korea. [10]Department of MetaBioHealth, Institute for ICS, Sungkyunkwan University, Suwon 16419, Republic of Korea.

Received: 1 November 2024 Accepted: 29 April 2025
Published online: 26 May 2025

References

1. Raslan AA, Pham TX, Lee JS, Kontodimas K, Tilston-Lunel A, Schmottlach J, Hong JM, Dinc T, Bujor AM, Caporarello N, et al. Lung injury-induced activated endothelial cell states persist in aging-associated progressive fibrosis. Nat Commun. 2024. https://doi.org/10.1038/s41467-024-49545-x.
2. Bonella F, Spagnolo P, Ryerson C. Current and future treatment landscape for idiopathic pulmonary fibrosis. Drugs. 2023;83:1581–93.
3. Liu SA, Su XL, Pan PH, Zhang LM, Hu YB, Tan HY, Wu DD, Liu B, Li HT, Li HS, et al. Neutrophil extracellular traps are indirectly triggered by lipopolysaccharide and contribute to acute lung injury. Sci Rep. 2016. https://doi.org/10.1038/srep37252.
4. Ambardar SR, Hightower SL, Huprikar NA, Chung KK, Singhal A, Collen JF. Post-COVID-19 pulmonary fibrosis: novel sequelae of the current pandemic. J Clin Med. 2021;10:2452.
5. Brinkmann V, Reichard U, Goosmann C, Fauler B, Uhlemann Y, Weiss DS, Weinrauch Y, Zychlinsky A. Neutrophil extracellular traps kill bacteria. Science. 2004;303:1532–5.
6. Kamiya M, Carter H, Espindola MS, Doyle TJ, Lee JS, Merriam LT, Zhang F, Kawano-Dourado L, Sparks JA, Hogaboam CM, et al. Immune mechanisms in fibrotic interstitial lung disease. Cell. 2024;187:3506–30.
7. Shafqat A, Omer MH, Albalkhi I, Razzak GA, Abdulkader H, Rab SA, Sabbah BN, Alkattan K, Yaqinuddin A: Neutrophil extracellular traps and long COVID. *Frontiers in Immunology* 2023, 14.
8. Varughese A, Balnadupete A, Ramesh P, Prasad TSK, Nidha AB, Bhandary Y. Guardians Turned Culprits: NETosis and Its Influence on Pulmonary Fibrosis Development. Mol Biotechnol. 2024;67:1752.
9. Lin H, Liu J, Li N, Zhang B, Nguyen VD, Yao P, Feng J, Liu Q, Chen Y, Li G, et al. NETosis promotes chronic inflammation and fibrosis in systemic lupus erythematosus and COVID-19. Clin Immunol. 2023;254: 109687.
10. Chen J, Wang T, Li X, Gao L, Wang K, Cheng M, Zeng Z, Chen L, Shen Y, Wen F. DNA of neutrophil extracellular traps promote NF-kappaB-dependent autoimmunity via cGAS/TLR9 in chronic obstructive pulmonary disease. Signal Transduct Target Ther. 2024;9:163.
11. Jiménez-Alcázar M, Rangaswamy C, Panda R, Bitterling J, Simsek YJ, Long AT, Bilyy R, Krenn V, Renné C, Renné T, et al. Host DNases prevent vascular occlusion by neutrophil extracellular traps. Science. 2017;358:1202.
12. Okeke EB, Louttit C, Fry C, Najafabadi AH, Han K, Nemzek J, Moon JJ. Inhibition of neutrophil elastase prevents neutrophil extracellular trap formation and rescues mice from endotoxic shock. Biomaterials. 2020;238: 119836.
13. Myllarniemi M, Kaarteenaho R. Pharmacological treatment of idiopathic pulmonary fibrosis-preclinical and clinical studies of pirfenidone, nintedanib, and *N*-acetylcysteine. Eur Clin Respir J. 2015;2: 263865.
14. Raghu G, Johnson WC, Lockhart D, Mageto Y. Treatment of idiopathic pulmonary fibrosis with a new antifibrotic agent, pirfenidone—results of a prospective, open-label phase II study. Am J Respir Crit Care Med. 1999;159:1061–9.
15. Ju KY, Lee Y, Lee S, Park SB, Lee JK. Bioinspired polymerization of dopamine to generate melanin-like nanoparticles having an excellent free-radical-scavenging property. Biomacromol. 2011;12:625–32.
16. Park J, Wysocki RW, Amoozgar Z, Maiorino L, Fein MR, Jorns J, Schott AF, Kinugasa-Katayama Y, Lee Y, Won NH, et al. Cancer cells induce metastasis-supporting neutrophil extracellular DNA traps. Sci Transl Med. 2016;8: 361ra138.
17. Lee NK, Wang CJ, Lim J, Park W, Kwon HK, Kim SN, Kim TH, Park CG. Impact of the conjugation of antibodies to the surfaces of polymer nanoparticles on the immune cell targeting abilities. Nano Converg. 2021;8:24.
18. Schmid D, Park CG, Hartl CA, Subedi N, Cartwright AN, Puerto RB, Zheng YR, Maiarana J, Freeman GJ, Wucherpfennig KW, et al. T cell-targeting nanoparticles focus delivery of immunotherapy to improve antitumor immunity. Nat Commun. 2017. https://doi.org/10.1038/s41467-017-01830-8.
19. Lee YY, Park HH, Park W, Kim H, Jang JG, Hong KS, Lee JY, Seo HS, Na DH, Kim TH, et al. Long-acting nanoparticulate DNase-1 for effective suppression of SARS-CoV-2-mediated neutrophil activities and cytokine storm. Biomaterials. 2021;267: 120389.
20. Park HH, Park W, Lee YY, Kim H, Seo HS, Choi DW, Kwon HK, Na DH, Kim TH, Choy YB, et al. Bioinspired DNase-I-coated melanin-like nanospheres for modulation of infection-associated NETosis dysregulation. Adv Sci (Weinh). 2020;7:2001940.
21. Wang CJ, Ko GR, Lee YY, Park J, Park W, Park TE, Jin Y, Kim SN, Lee JS, Park CG. Polymeric DNase-I nanozymes targeting neutrophil extracellular traps for the treatment of bowel inflammation. Nano Converg. 2024;11:6.
22. Schmid D, Park CG, Hartl CA, Subedi N, Cartwright AN, Puerto RB, Zheng Y, Maiarana J, Freeman GJ, Wucherpfennig KW, et al. T cell-targeting nanoparticles focus delivery of immunotherapy to improve antitumor immunity. Nat Commun. 2017;8:1747.
23. Aktan MK, Van der Gucht M, Hendrix H, Vande Velde G, Baert K, Hauffman T, Killian MS, Lavigne R, Braem A. Anti-infective DNase I coatings on polydopamine functionalized titanium surfaces by alternating current electrophoretic deposition. Anal Chim Acta. 2022;1218: 340022.
24. Park HH, Park W, Lee YY, Kim H, Seo HS, Choi DW, Kwon HK, Na DH, Kim TH, Choy YB, et al. Bioinspired DNase-I-coated melanin-like nanospheres for modulation of infection-associated NETosis dysregulation. Adv Sci (Weinh). 2021;8: e2103748.
25. Tang YX, Fan ZW, Li J, Pan HD, Su WX, Matniyaz Y, Zhang HT, Luo YX, Lv ZK, Wang WZ, et al. Sivelestat in patients at a high risk of postoperative acute lung injury after scheduled cardiac surgery: a prospective cohort study. J Inflamm Res. 2024;17:591–601.
26. Peluso MJ, Deitchman AN, Torres L, Iyer NS, Munter SE, Nixon CC, Donatelli J, Thanh C, Takahashi S, Hakim J, et al. Long-term SARS-CoV-2-specific immune and inflammatory responses in individuals recovering from COVID-19 with and without post-acute symptoms. Cell Rep. 2021;36: 109518.

Publisher's Note